A Variational Method for Analyzing Vortex Flows in Radar-Scanned Tornadic Mesocyclones. Part III: Sensitivities to Vortex Center Location Errors

QIN XU[a] AND LI WEI[b]

[a] *NOAA/OAR/National Severe Storms Laboratory, Norman, Oklahoma*
[b] *Cooperative Institute for Severe and High-Impact Weather Research and Operations, University of Oklahoma, Norman, Oklahoma*

(Manuscript received 28 July 2021, in final form 4 February 2022)

ABSTRACT: When the vortex center location is estimated from a radar-scanned tornadic mesocyclone, the estimated location is not error-free. This raises an important issue concerning the sensitivities of analyzed vortex flow (VF) fields by the VF-Var (formulated in Part I of this paper series and tested in Part II) to vortex center location errors, denoted by $\Delta\mathbf{x}_c$. Numerical experiments are performed to address this issue with the following findings: The increase of $|\Delta\mathbf{x}_c|$ from zero to a half of vortex core radius causes large analysis error increases in the vortex core but the increased analysis errors decrease rapidly away from the vortex core especially for dual-Doppler analyses. The increased horizontal-velocity errors in the vortex core are mainly in the $\Delta\mathbf{x}_c$-normal component, because this component varies much more rapidly than the other component along the $\Delta\mathbf{x}_c$ direction in the vortex core. The vertical variations of $\Delta\mathbf{x}_c$ distort the vertical correlation structure of $\Delta\mathbf{x}_c$-dislocated VF-dependent background error covariance, which can increase the analysis errors in the vortex core. The dual-Doppler analyses have adequate accuracies outside the vortex core even when $|\Delta\mathbf{x}_c|$ increases to a half of vortex core radius, while single-Doppler analyses can also have adequate accuracies outside the vortex core mainly for the single-Doppler-observed velocity component. The sensitivities to $\Delta\mathbf{x}_c$ are largely unaffected by the vortex slanting. The above findings are important and useful for assessing the accuracies of analyzed VFs for real radar-observed tornadic mesocyclones.

SIGNIFICANCE STATEMENT: When the vortex center location is estimated from a radar-scanned tornadic mesocyclone, the estimated location is not error-free. This raises an issue concerning the sensitivity of analyzed vortex flow (VF) by the VF-Var (formulated in Part I of this paper series and tested with simulated radar observations in Part II) to vortex center location error. This issue and its required investigations are very important for the VF-Var to be applied to real radar-observed tornadic mesocyclones, especially in an operational setting with the WSR-88Ds. Numerical experiments are performed to address this issue. The findings from these experiments are important and useful for assessing the accuracies of VF-Var analyzed VF fields for real radar-observed tornadic mesocyclones.

KEYWORDS: Mesocyclones; Vortices; Radars/Radar observations; Error analysis; Variational analysis; Data assimilation

1. Introduction

To increase warning lead times for tornados, severe thunderstorms, damaging winds, and flash floods, great efforts have been made with successive progresses at the National Severe Storms Laboratory (NSSL) in developing a Warn-on-Forecast system with variational, ensemble, and ensemble–variational-hybrid data assimilation capabilities (Stensrud et al. 2009, 2013; Gao et al. 2013; Gao and Stensrud 2014; Wheatley et al. 2015; Jones et al. 2016; Yussouf et al. 2016, 2020; Skinner et al. 2018; Lawson et al. 2018; Wang et al. 2019). However, analyzing three-dimensional (3D) vortex flow (VF) fields in radar-observed tornadic mesocyclones remains extremely difficult but critical for tornadic-storm data assimilation and forecasts (Snook et al. 2019). To attack this difficult task, a variational method, called VF-Var, was formulated (Xu 2021, hereafter Part I) by extending the two-dimensional VF-dependent covariance functions of Xu et al. (2015a) to 3D versions. As these 3D VF-dependent covariance functions were constructed in a vortex-following slantwise cylindrical coordinate system (with its vertical coordinate given, as a function of height and time, by the estimated vortex center axis), they overcome the intrinsic limitation encountered by the previously developed variational methods at NSSL (Gao et al. 2013; Xu et al. 2010, 2015b) in analyzing small-scale vortex winds due to the use of horizontally isotropic background error covariance formulations. This implies that the previously developed variational methods can be improved in analyzing small-scale vortex winds by using these 3D VF-dependent covariance functions to perform an additional step of small-scale analysis locally. Alternatively, the VF-Var can be used first to analyze vortex winds, and its analyzed vortex winds can be then used as "observations" (with properly specified error variances) in the previously developed variational methods to improve their analyses of small-scale vortex winds.

This VF-Var was tested by Xu and Wei (2021, hereafter Part II) with simulated radar radial-velocity scans of analytically formulated benchmark vortices [but two typos in (A1a)–(A2b) of Part II were overlooked during proofreading: $(1 + R^4)/R_1^4$ and $(1 + R^4)/R_2^4$ should be $1 + R^4/R_1^4$ and $1 + R^4/R_2^4$, respectively]. The test experiments demonstrated that the

Corresponding author: Qin Xu, qin.xu@noaa.gov

DOI: 10.1175/JAS-D-21-0203.1

VF-Var performed very well (or reasonably well) with dual-Doppler (or single-Doppler) scans, and errors in the analyzed velocities from single-Doppler scans were mainly in the unobserved velocity components and only in fractions of the benchmark velocities. In these test experiments, the vortex center location is assumed to be accurately estimated. However, when the vortex center location is estimated as a continuous function of height and time from Doppler scans of a real tornadic mesocyclone by using the three-step method of Xu et al. (2017), the estimated vortex center location is not free of error (due to the limited spatial and temporal resolutions of radar scans and the intrinsic uncertainty of true vortex center location) although the error can be only a fraction of the radius of vortex core. Thus, it is unknown how small errors in the estimated vortex center locations affect the accuracies of analyses produced by the VF-Var. This issue will be addressed in this paper.

As a follow-up of Part II, this paper designs and performs additional numerical experiments to examine the sensitivities of analyses produced by the VF-Var to vortex center location errors. In these sensitivity experiments, simulated radial-velocity observations will be generated from idealized and pseudo-operational Doppler scans of analytically formulated vortices in the same way as in Part II but small errors (up to a half of the radius of the vortex core) will be considered in the estimated vortex center axis that defines the vertical coordinate of the analysis domain. The VF-Var can be performed with the axisymmetric and asymmetric parts of VF analyzed either simultaneously in a single step or sequentially in two steps (see their algorithm flowcharts in Fig. 4 of Part I). Since these two approaches have similar sensitivities to the true vortex center location, the sensitivity experiment results will be presented only for the single-step approach in this paper.

The paper is organized as follows: Section 2 designs numerical experiments for studying the concerned sensitivities. Sections 3 and 4 present and examine the results of experiments performed with idealized and pseudo-operational Doppler scans, respectively. Conclusions follow in section 5.

2. Experiment design

a. Experiments with idealized Doppler scans

As described in section 2b of Part II, the idealized Doppler scans measure only the horizontal components of 3D velocities on a coarse-resolution grid in the analysis domain, but here the analysis domain is no longer cocentered with the benchmark vortex for the test experiments designed later. The upright and eastward-slantwise benchmark vortices formulated by setting $\partial_z \mathbf{x}_c = (0, 0)$ and $(0.5, 0)$, respectively, in Part II are used again for the sensitivity experiments designed below with idealized Doppler scans, where $\mathbf{x}_c \equiv (x_c, y_c)$ denotes the true vortex center location which is a vector function of (z, t) in the local Cartesian coordinate system (x, y, z, t) as explained in Part I, and $\partial_z \mathbf{x}_c = (\partial_z x_c, \partial_z y_c)$ is the slope of true vortex center axis in the physical space.

The sensitivity experiments with each (upright or eastward-slantwise) vortex consist of three sets corresponding to the three types of idealized Doppler scans described in sections 2b and 3b of Part II; that is, (i) the dual-Doppler scans that generate $(-u^o, v^o)$ observations, (ii) the single-Doppler scans that generate $-u^o$ observations, and (iii) the single-Doppler scans that generate v^o observations [see (2.3) of Part II]. These idealized observations are generated on a coarse-resolution grid in the analysis domain with $\Delta x' = \Delta y' = 0.5$ km at five vertical levels, every $\Delta z' = 1$ km, from $z' = 1$ to 5 km. Here, (x', y', z', t') is the vortex-following coordinate system defined by

$$(x', y', z', t') \equiv (x - x_c^e, y - y_c^e, z, t), \tag{2.1}$$

as in (2.1) of Part I but with $\mathbf{x}_c$ replaced by $\mathbf{x}_c^e \equiv (x_c^e, y_c^e)$, where $\mathbf{x}_c^e$ denotes the estimated vortex center location which is also a vector function of (z, t). Each set of experiments consists of one control experiment and two test experiments. The control experiment in the first (second or third) set is same as the experiment E-uv-1 (E-u-1 or E-v-1) performed with the single-step approach in Part II, in which $\mathbf{x}_c^e = \mathbf{x}_c$ so $\Delta \mathbf{x}_c \equiv \mathbf{x}_c^e - \mathbf{x}_c = (\Delta x_c, \Delta y_c) = (0, 0)$. The first (or second) test experiment is similar to the control experiment in each set but $\mathbf{x}_c^e$ is deviated from $\mathbf{x}_c$ eastward by $\Delta x_c \equiv x_c^e - x_c = R_1/4$ (or $R_1/2$), where R_1 (=1 km) is the vortex core radius (defined by the radius of maximum axisymmetric tangential velocity of VF). Thus, in the first (or second) test experiment, the analysis domain and its coordinate system (x', y', z') are deviated from their benchmark counterparts by $\Delta x_c = R_1/4$ (or $R_1/2$).

Here, $\Delta \mathbf{x}_c$ is set to $(\Delta x_c, 0)$ as a vertically uniform and unidirectional vector function of z to facilitate later detailed analyses and gain physical insights on how the deviations of $\mathbf{x}_c^e$ from $\mathbf{x}_c$ affect the accuracies of different component fields of analyzed velocity especially around the estimated vortex center. The aforementioned control experiments in the first, second, and third sets are renamed (from E-uv-1, E-u-1, and E-v-1 named in Part II) to E-uv-T0, E-u-T0, and E-v-T0, respectively, while the first (or second) test experiments in the first, second, and third sets are named E-uv-T1, E-u-T1, and E-v-T1 (or E-uv-T2, E-u-T2, and E-v-T2), respectively.

b. Experiments with pseudo-operational Doppler scans

This subsection describes the design of sensitivity experiments with pseudo-operational Doppler scans of upright and slanted vortices. As described in section 2b of Part II, the pseudo-operational Doppler scans mimic the scan mode VCP12 used by operational WSR-88D radars for severe storms. In this mode, a full volume of radial velocity is scanned from each radar on 14 sweeps (from 0.5° to 19.5°) over the analysis time window from $t = 0$ to 5 min, while the range resolution is 250 m and the azimuthal beam spacing is 0.5°. The first radar, called radar A (or the second radar, called radar B) is 30 km to the east (or south) of the estimated vortex center on the ground ($z = 0$) at $t = 0$. The estimated vortex center $\mathbf{x}_c^e$ for the upright (or eastward-slantwise) vortex is formulated in the same way as that described in section 2b and shown in Fig. 2 of Part II with $\partial \mathbf{x}_c^e = (\partial_z x_c^e, \partial_z y_c^e) = (0, 0)$ [or $(0.5, 0)$].

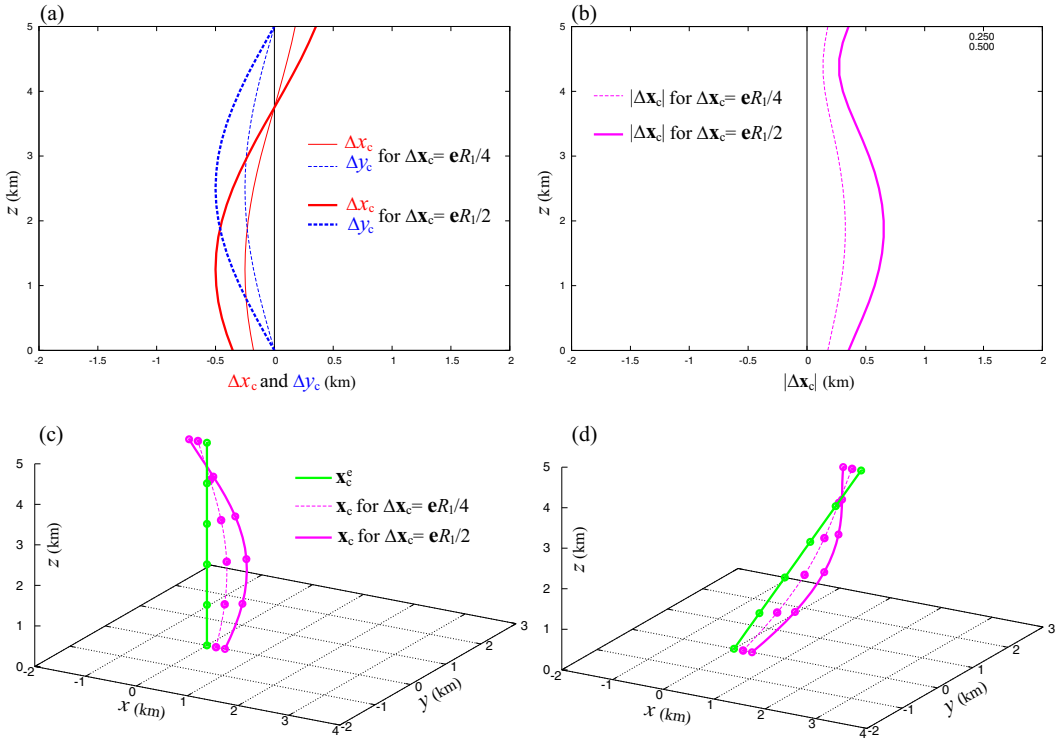

FIG. 1. (a) Vertical profiles of $\Delta\mathbf{x}_c = \mathbf{e}R_1/4$ (or $\mathbf{e}R_1/2$) plotted by thin (or thick) solid red and dashed blue curves for x and y components, respectively, where $R_1 = 1$ km is the radius of the vortex core and $\mathbf{e}$ is defined in (2.2). (b) Vertical profiles of $|\Delta\mathbf{x}_c| = |\mathbf{e}|R_1/4$ (or $|\mathbf{e}|R_1/2$) plotted by dashed (or solid) purple curve. (c) 3D perspectives of $\mathbf{x}_c^e$ and $\mathbf{x}_c = \mathbf{x}_c^e - \Delta\mathbf{x}_c$,with $\Delta\mathbf{x}_c = \mathbf{e}R_1/4$ (or $\mathbf{e}R_1/2$) plotted by solid green and dashed (or solid) purple curves, respectively, for the upright vortex in original physical coordinates (x, y, z) cocentered with $\mathbf{x}_c^e$. (d) As in (c), but for the eastward-slanted vortex in original physical coordinates (x, y, z) cocentered with $\mathbf{x}_c^e$ at $z = 0$.

The sensitivity experiments with each (upright or eastward-slantwise) vortex consist of three sets corresponding to the three types of pseudo-operational Doppler scans described in section 3b of Part II: that is, (i) the dual-Doppler scans from radar A and radar B, (ii) the single-Doppler scans from radar A only, and (iii) the single-Doppler scans from radar B only. Each set consists of one control experiment and two test experiments. The control experiment in the first (second or third) set is same as the experiment E-AB-1 (E-A-1 or E-B-1) performed in Part II with $\mathbf{x}_c^e = \mathbf{x}_c$. The first (or second) test experiment is similar to the control experiment in each set except that $\mathbf{x}_c{}^e$ deviates from $\mathbf{x}_c$ by $\Delta\mathbf{x}_c = \mathbf{e}R_1/4$ (or $\mathbf{e}R_1/2$), where $\mathbf{e}$ is a vector function of z defined by

$$\mathbf{e} \equiv \left[-\cos(\pi z/D - \pi/4),\ -\sin(\pi z/D)\right], \tag{2.2}$$

and $D = 5$ km is the analysis domain height (determined by the radar-observed height of VF as explained in appendix A of Part II). The benchmark vortex center is thus given by $\mathbf{x}_c = \mathbf{x}_c^e - \Delta\mathbf{x}_c$. Figure 1a (or Fig. 1b) shows the vertical profiles of Δx_c and Δy_c (or $|\Delta\mathbf{x}_c|$) used for the two test experiments in each set. Figure 1c (or Fig. 1d) shows a three-dimensional view of the vertical profiles of $\mathbf{x}_c^e$ and $\mathbf{x}_c$ used for the two test experiments in the first (or second) set for the upright (or eastward-slantwise) vortex. Note that a real tornado usually has a smooth vortex core (as often indicated by its visible smooth condensation funnel) and the vortex center axis is estimated also as a smooth vector function of z (by using the three-step method of Xu et al. 2017), so $\Delta\mathbf{x}_c$ is also a smooth vector function of z. Thus, for simplicity, the two components of $\Delta\mathbf{x}_c$ can be represented by sinusoidal functions as shown in (2.2).

Here, by using $\mathbf{e}$ defined in (2.2), $\Delta\mathbf{x}_c$ is a vertically varying vector function of z, so it can mimic the error of vortex center location estimated from Doppler scans of a real tornadic mesocyclone by using the three-step method of Xu et al. (2017). The aforementioned control experiments in the first, second, and third sets are renamed (from E-AB-1, E-A-1, and E-B-1 named in Part II) to E-AB-T0, E-A-T0, and E-B-T0, respectively, while the first (or second) test experiments in the first, second, and third sets are named E-AB-T1, E-A-T1, and E-B-T1 (or E-AB-T2, E-A-T2, and E-B-T2), respectively.

c. *Evaluation methods*

The cylindrical-volume-averaged RMS error (CRE), relative CRE (RCRE), area-averaged RMS error (ARE), domain-averaged RMS error (DRE) and relative DRE (RDRE) defined in Part II are reintroduced here and will be used again in this paper to evaluate the accuracies of analyzed (u', v', w'),

TABLE 1. List and descriptions of acronyms of error metrics reintroduced in section 2c for evaluating the accuracies of analyzed (u', v', w') in (x', y', z').

Acronym	Description
ARE	Area-averaged RMS error—A function of z', with the area average taken over the entire 20×20 km^2 area of the analysis domain for given z'
CRE	Cylindrical-volume-averaged RMS error with cylindrical-volume average taken over the volume within 5-km radial distance from the estimated vortex center through the entire 5-km depth of the analysis domain
DRE	Domain-averaged RMS error with domain average taken over the entire $20 \times 20 \times 5$ km^3 volume of the analysis domain
RCRE	Relative CRE—The ratio (in %) of CRE to cylindrical-volume-averaged RMS value of the related benchmark field
RDRE	Relative DRE—The ratio (in %) of DRE to domain-averaged RMS value of the related benchmark field

where $(u', v', w') \equiv d_t(x', y', z')$ is the contravariant velocity of VF in (x', y', z') as defined in Table 1 of Part I. This contravariant velocity is related to the total velocity, (u, v, w), in the original Cartesian coordinate system (x, y, z) by

$$(u', v', w') = (u - \partial_t x_c^e - w\partial_z x_c^e, v - \partial_t y_c^e - w\partial_z y_c^e, w). \quad (2.3)$$

Here, (2.3) is derived in the same way as (2.2) in Part I except that (x_c, y_c) is replaced by (x_c^e, y_c^e). Note that $(\partial_t x_c^e, \partial_t y_c^e)$ is the estimated vortex center moving velocity. This estimated moving velocity can be accurate enough (to not significantly affect the VF-Var) and thus assumed to be error-free in this paper. As listed and described in Table 1, the area average is taken over the entire 20×20 km^2 area of the analysis domain for given z', the cylindrical-volume average is taken over the volume within 5 km radial distance from the estimated vortex center through the entire depth (from $z' = 0$ to 5 km) of the analysis domain, the domain average is taken over the entire volume of the analysis domain, the RCRE is defined as the ratio (in percentage) of CRE to the cylindrical-volume-averaged RMS value of the related benchmark field, and the RDRE is defined as the ratio (in percentage) of DRE to the domain-averaged RMS value of the related benchmark field.

As in Part II, the analysis domain is centered at $(x', y') = (0, 0)$ along the z' coordinate (from $z' = 0$ to 5 km) and covers a square area of 20×20 km^2 at each vertical level, but (x', y', z') is the coordinate system cocentered with the estimated vortex center axis (that coincides with the benchmark vortex center axis only when $\Delta\mathbf{x}_c$ is zero in each control experiment). Also as in Part II, the horizontal and vertical grid resolutions for computing the aforementioned RMS errors are set to $\Delta x' = \Delta y' = 0.25$ km and $\Delta z' = 0.5$ km, respectively, which are finer than the smallest background error decorrelation length and depth, respectively, and roughly match the highest horizontal and vertical resolutions of nonuniformly distributed observations from the pseudo-operational Doppler scans.

TABLE 2. CREs and RCREs of analyzed (u', v', w') from experiments performed with idealized Doppler scans of the upright vortex in section 3a. As explained in section 2a, each experiment is named in three parts. The letter "uv," "u," or "v" in the middle part means that the experiment is performed with the dual-Doppler observations given by $(-u^o, v^o)$, the single-Doppler observations given by $-u^o$ only, or the single-Doppler observations given by v^o only. The letter "T0," "T1," or "T2" in the last part means that the experiment is performed by setting $\Delta x_c = 0$, $R_1/4$ or $R_1/2$ with $\Delta\mathbf{x}_c = (\Delta x_c, 0)$, where $\Delta\mathbf{x}_c$ denotes the vector deviation of the estimated vortex center from the benchmark vortex center, and $R_1 = 1$ km is the radius of vortex core. Thus, E-uv-T0, E-u-T0, and E-v-T0 are the control experiments that duplicate E-uv-1, E-u-1, and E-v-1 performed with the single-step approach in section 4a and listed in Table 2 of Part II.

		CRE (m s^{-1})			RCRE (%)		
Expt	Δx_c	u'	v'	w'	u'	v'	w'
E-uv-T0	0	0.8	0.6	2.9	5	4	31
E-uv-T1	$R_1/4$	1.2	1.8	3.2	8	11	34
E-uv-T2	$R_1/2$	1.8	3.0	3.9	12	20	41
E-u-T0	0	0.7	2.2	3.1	5	15	33
E-u-T1	$R_1/4$	1.1	3.4	3.8	7	22	40
E-u-T2	$R_1/2$	1.8	5.5	5.0	12	36	54
E-v-T0	0	3.9	0.6	3.5	26	4	37
E-v-T1	$R_1/4$	4.1	1.7	4.3	27	11	46
E-v-T2	$R_1/2$	4.6	3.0	5.5	30	20	58

3. Sensitivity experiments with idealized Doppler scans

a. Results for upright vortex

1) EXPERIMENTS WITH IDEALIZED DUAL-DOPPLER OBSERVATIONS

For the three experiments performed with idealized dual-Doppler $(-u^o, v^o)$ observations of the upright vortex, the CREs and RCREs of analyzed (u', v', w') are shown in rows 1–3 of Table 2. As shown, when Δx_c increases from 0 to $R_1/4$ (or $R_1/2$), the CRE is increased from 0.8 to 1.2 (or 1.8) m s^{-1} roughly by 50% (or 140%) for u', from 0.6 to 1.8 (or 3.0) m s^{-1} roughly by 180% (or 380%) for v', and from 2.9 to 3.2 (or 3.9) m s^{-1} roughly by 10% (or 30%) for w'. Clearly, the CRE is increased with Δx_c more rapidly for v' than for u'. This is because v' varies rapidly along the x' direction in the vortex core and changes sign across the vortex center but u' is nearly zero along the x' coordinate and varies much less rapidly than v' along the x' direction in the vortex core. Thus, the errors of analyzed $\mathbf{u}' \equiv (u', v')$ caused by the x'-directional deviation of $\mathbf{x}_c^e$ from $\mathbf{x}_c$ are mainly in the v' component in the vortex core. Also as shown in Table 2, the RCREs for (u', v') are below 5% from E-uv-T0 and increased to (12, 20)% when Δx_c increases to $R_1/2$ in E-uv-T2. In contrast, the RCRE for w' is 31% in E-uv-T0 but increased only to 41% in E-uv-T2.

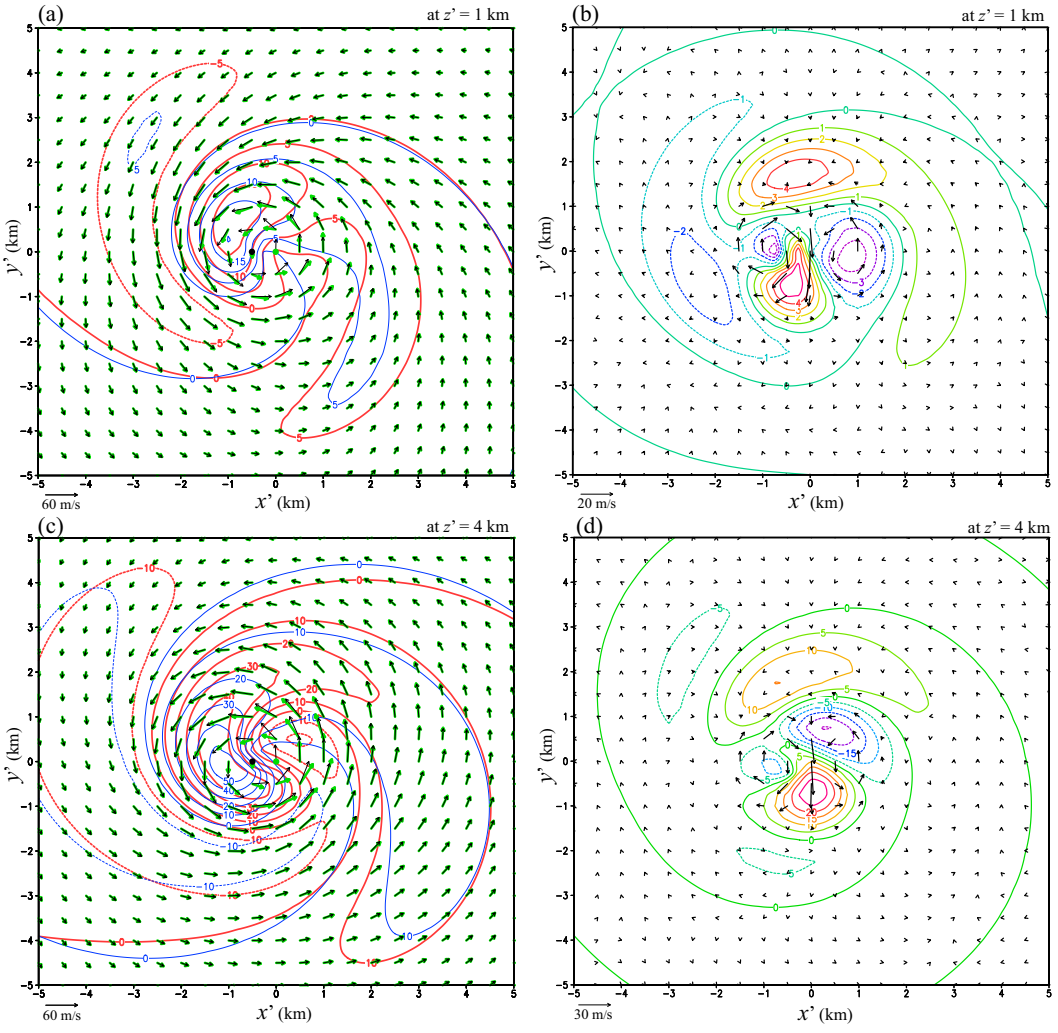

FIG. 2. (a) Analyzed $\mathbf{u}' \equiv (u', v')$ and w' at $z' = 1$ km from E-uv-T2 performed with dual-Doppler $(-u^o, v^o)$ observations of the upright vortex plotted by thick green arrows and thick red contours, respectively, vs their benchmark $\mathbf{u}'$ and w' plotted by black arrows and thin blue contours, respectively. (b) As in (a), but for the errors of analyzed $\mathbf{u}'$ and w' at $z' = 1$ km plotted by black arrows and color contours, respectively. (c) As in (a), but at $z' = 4$ km. (d) As in (b), but at $z' = 4$ km. The vector scale is shown at the lower-left corner in each panel. In (a) and (c), the green dot marks the estimated vortex center at the domain center and the black dot marks the benchmark vortex center, so $\Delta\mathbf{x}_c$ is the vector distance from the black dot to the domain center—the estimated vortex center marked by the green dot.

Figures 2a and 2c show the analyzed $\mathbf{u}' \equiv (u', v')$ and w' from E-uv-T2 against their respective benchmark fields in the central area (confined by $|x'| \le 5$ km and $|y'| \le 5$ km) of the analysis domain at $z' = 1$ and 4 km, respectively, while their corresponding error fields are shown in Figs. 2b and 2d, respectively. [Outside the 10×10 km^2 central area, the dual-Doppler analyzed $(\mathbf{u}', w')$ are very close to their respective benchmark fields and the differences are too small to clearly display over the entire 20×20 km^2 analysis domain, so the dual-Doppler analyzed $(\mathbf{u}', w')$ are plotted against their respective benchmark fields only in the central area in Fig. 2.] As shown, errors of analyzed $\mathbf{u}'$ and w' are large in the vortex core (defined by $R \le R_1 = 1$ km where R is the radial distance from the estimated vortex center) but decrease rapidly away from the vortex core and become negligibly small as R increases to and beyond 2.5 km. Large errors of analyzed $\mathbf{u}'$ in the vortex core are mainly in v'-component velocities, so the CRE increases with Δx_c more rapidly for v' than for u' as seen earlier in rows 1–3 of Table 2.

As shown in Fig. 2a (or Fig. 2c), the benchmark $\mathbf{u}'$ is 23 (or 31) m s^{-1} northward at the domain center and so is the observed $\mathbf{u}'$, but the analyzed $\mathbf{u}'$ is constrained by the VF-Var to vanish at the domain center—the estimated vortex center denoted by the green dot. The benchmark vortex center is denoted by the black dot at $(x', y') = (-0.5, 0)$ km, where the benchmark $\mathbf{u}'$ vanishes but the analyzed $\mathbf{u}'$ is 10.7 (or 11.3) m s^{-1} southward in Fig. 2a (or Fig. 2c). Away from the estimated vortex center, $\mathbf{u}'$ is estimated from weighted observations (with the

weights determined mainly by the VF-dependent background error correlation) over a semicircular volume (extended from the reference point where $\mathbf{u}'$ is estimated) around the estimated vortex center axis. This explains why the analyzed $\mathbf{u}'$ is nonzero at the benchmark vortex center, as seen in Fig. 2a (or Fig. 2c) or seen more clearly in Fig. 2b (or Fig. 2d).

Furthermore, when the reference point is in the estimated vortex core, the aforementioned semicircular volume is small and tightly around the estimated vortex center axis, so its geometric connection to the true vortex center is severely affected by the deviation of the estimated vortex center from the true vortex center. Conversely, when the reference point is far outside the estimated vortex core, the aforementioned semicircular volume is large and distantly around the estimated vortex center axis, so its geometric connection to the true vortex center is slightly affected by the deviation of the estimated vortex center from the true vortex center. This location-dependent (relative to the estimated vortex center) geometric connection explains why the error of analyzed $\mathbf{u}'$ is large in the estimated vortex core but decreases rapidly away from the estimated vortex core, as shown in Figs. 2b and 2d. Besides, although w' is not observed, the analyzed w' and $\mathbf{u}'$ are linked via the mass continuity [see (2.3), (3.2), and (4.3) of Part I] and so are their error fields (as revealed in Figs. 2b,d). This linkage explains why the error of analyzed w' is also large in the analyzed vortex core and decreases rapidly away from the vortex core. The error fields of analyzed $\mathbf{u}'$ (or w') from E-uv-T1 have nearly the same pattens as those from E-uv-T2 in Figs. 2b and 2d but their amplitudes are reduced by about (or nearly) 50%.

Because large analysis errors are concentrated in and around the estimate vortex core, the DRE is smaller than half of the CRE for each analyzed field in each test experiment. In particular, the DREs are (0.6, 0.8, 1.4) m s^{-1} [or (0.9, 1.4, 1.7) m s^{-1}] for (u', v', w') from E-uv-T1 (or E-uv-T2). The domain-averaged RMS value is roughly half of the cylindrical-volume-averaged RMS value for each benchmark field, so the RDREs are (7%, 10%, 32%) [or (10%, 16%, 38%)] for (u', v', w') from E-uv-T1 (or E-uv-T2) which are slightly smaller than their corresponding RCREs in row 2 (or 3) of Table 2. The ARE is plotted as a function of z' in Fig. 3a for each analyzed field. The thin red (or green) curves in Fig. 3a show that as Δx_c increases from 0 to $R_1/4$ and then to $R_1/2$, the ARE of analyzed u' (or v') increases roughly from 0.25 to 0.5 (or 0.8) m s^{-1} and then to 0.8 (or 1.4) m s^{-1} above $z' = 1$ km, but the error increases are smaller for lower z' below 1 km [due to the lack of observation below $z' = 1$ km that causes the starting ARE of analyzed u' (or v') from E-uv-T0 to increase]. Clearly, the ARE increases with Δx_c more rapidly for v' than for u', and this is consistent with the earlier explained more rapid increase of CRE with Δx_c for v' than for u' in rows 1–3 of Table 2. The thick blue curves in Fig. 3a show that the ARE for w' is nearly unaffected (or only slightly affected) by the increase of Δx_c below (or above)

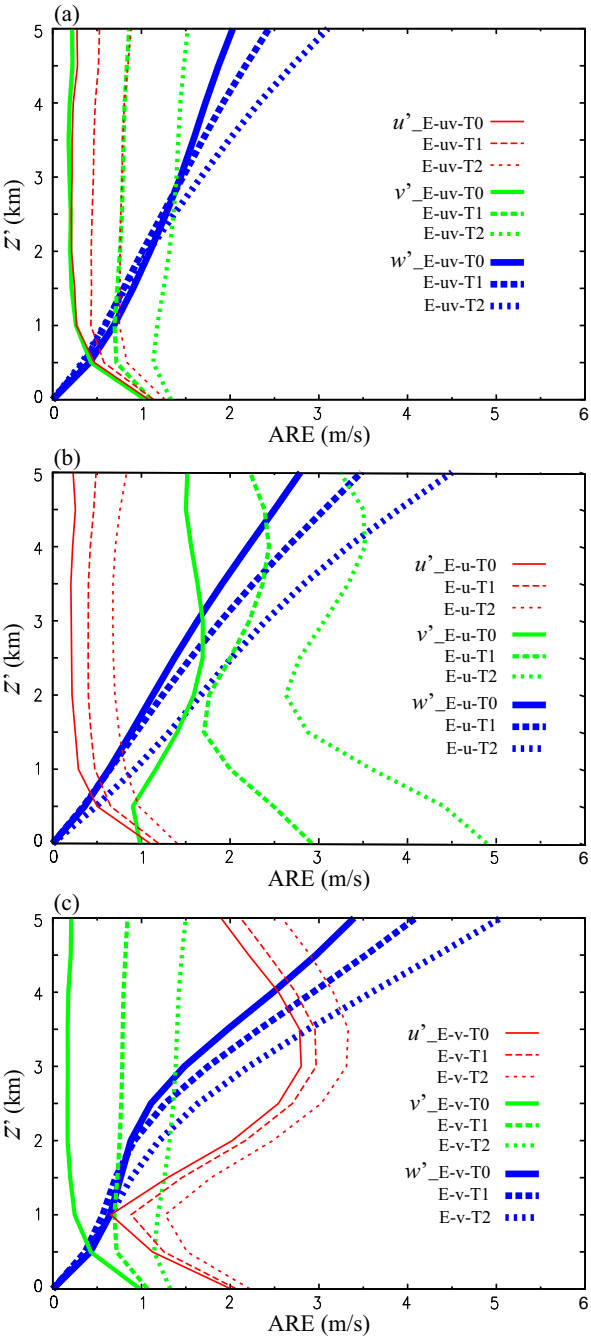

FIG. 3. ARE plotted as functions of z' for analyzed (u', v', w') from the three sets of experiments performed with idealized Doppler observations of the upright vortex in section 3a: (a) AREs plotted by solid, dashed, and dotted (thin red, green, thick blue) curves for analyzed (u', v', w') from E-uv-T0, E-uv-T1, and E-uv-T2, respectively, performed with dual-Doppler ($-u^o$, v^o) observations. (b) As in (a), but from E-u-T0, E-u-T1, and E-u-2 performed with single-Doppler $-u^o$ observations. (c) As in (a), but from E-v-T0, E-v-T1, and E-v-2 performed with single-Doppler v^o observations.

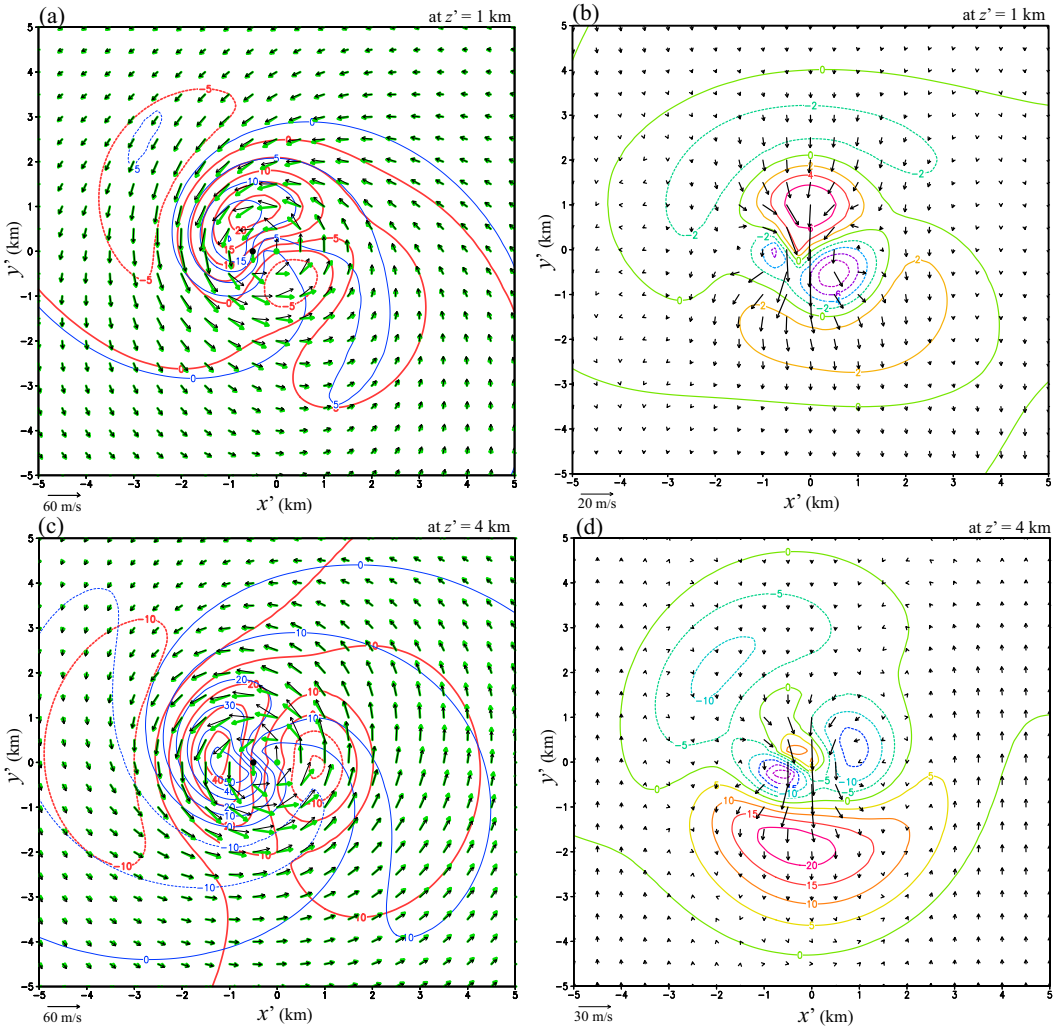

FIG. 4. As in Fig. 2, but from E-u-T2 performed with single-Doppler $-u^o$ observations of the upright vortex.

$z' = 3$ km. Thus, the analyzed (u', v') and w' both have adequate accuracies outside the vortex core even when Δx_c increases to $R_1/2$.

2) EXPERIMENTS WITH IDEALIZED SINGLE-DOPPLER OBSERVATIONS

Now the above idealized dual-Doppler $(-u^o, v^o)$ observations reduce to single-Doppler $-u^o$ observations. In this case, as shown in rows 4–6 versus rows 1–3 in Table 2, the CREs are nearly doubled for v' due to the absence of v^o, but the CREs are nearly unchanged for u' and increased slightly for w'. As the CRE for v' started from 2.2 m s^{-1} in E-u-T0, its corresponding RCRE is already 15% and thus is increased only to 36% in E-u-T2. Besides, since v' and its rapid variations in the vortex core are not observed, the analysis error of v' is less affected by the x'-directional deviation of $\mathbf{x}_c^e$ from $\mathbf{x}_c$. This also partially explains why the CRE for v' increases less rapidly with Δx_c in the absence of v^o.

Figures 4a–d show that the analyzed $\mathbf{u}'$ and w' from E-u-T2 deviate from their respective benchmark fields again largely in the vortex core, but the $\mathbf{u}'$ deviations are further dominated by v' deviations in the vortex core and decrease less rapidly away in the y (north–south) direction from the vortex core than in Fig. 2 due to the absence of v^o. The $\mathbf{u}'$ deviation at the domain center remains the same as in Fig. 2a (or Fig. 2c). The $\mathbf{u}'$ deviation at the benchmark vortex center is 20 (or 23) m s^{-1} southward in Fig. 4a (or Fig. 4c), which is larger than that in Fig. 2a (or Fig. 2c). This error is caused by the same reason as explained earlier for Fig. 2, but the analyzed v' is now much more negative than in Fig. 2 because the erroneous negative v' is no longer suppressed by v^o ($\approx$0 at the benchmark vortex center) due to the absence of v^o. Linked via the mass continuity, the error of analyzed w' also becomes larger and decreases less rapidly away from the vortex core due to the absence of v^o in E-u-T2, as shown in Figs. 4b and 4d versus Figs. 2b and 2d.

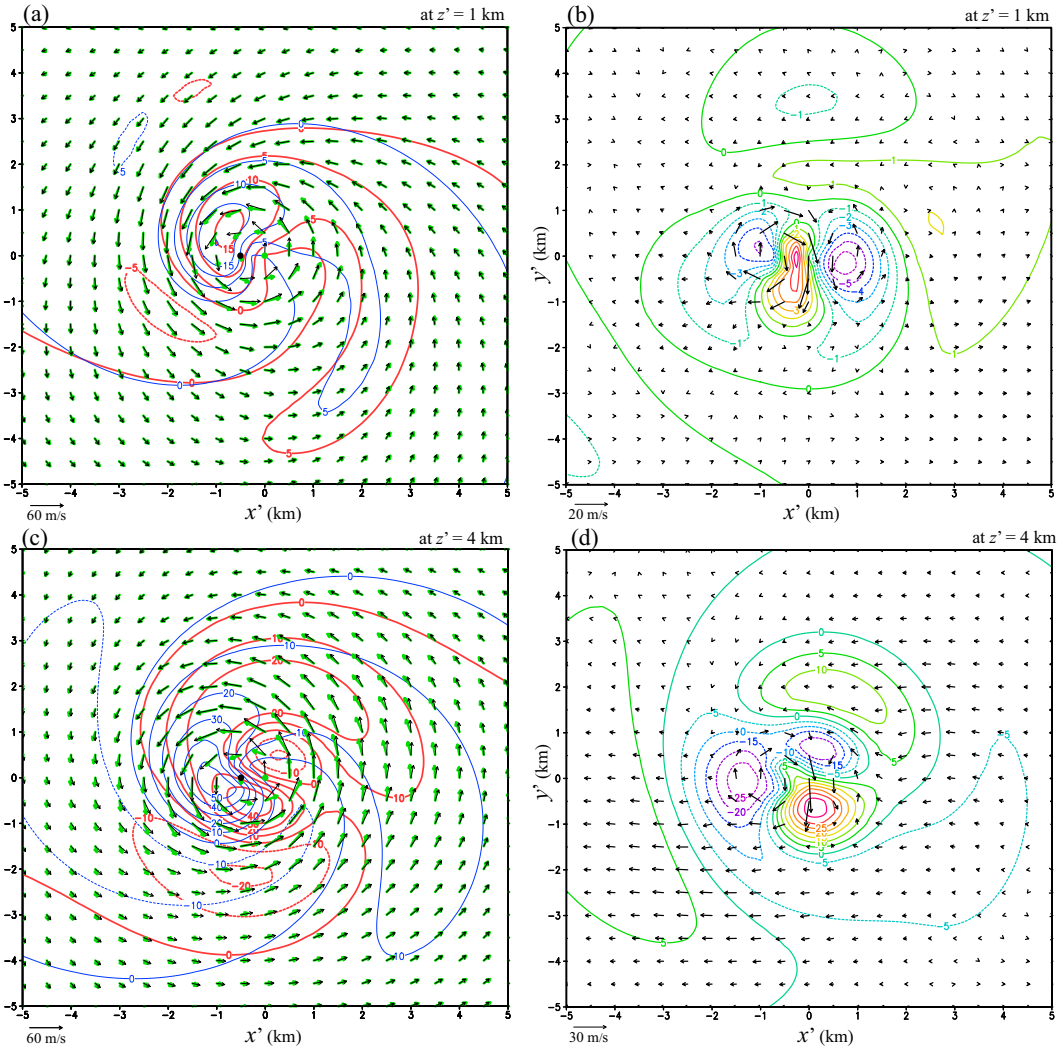

FIG. 5. As in Fig. 2, but from E-v-T2 performed with single-Doppler v^o observations of the upright vortex.

The AREs of analyzed (u', v', w') are plotted as functions of z' in Fig. 3b for E-u-T0, E-u-T1, and E-u-T2. Note that the three thin red curves in Fig. 3b are nearly identical to those in Fig. 3a, so the AREs for u' are virtually unaffected by the absence of v^o. However, as shown by the green curves in Fig. 3b versus those in Fig. 3a, the absence of v^o causes the ARE for v' to increase by about 1 m s^{-1} (or less) in E-u-T0, 1.5 m s^{-1} (or more) in E-u-T1, and 2 m s^{-1} (or more) in E-u-T2 above (or below) z' = 1 km. The absence of v^o also causes the AREs for w' to increase slightly, as shown by the thick blue curves in Fig. 3b versus those in Fig. 3a. Thus, when the ($-u^o$, v^o) observations reduce to $-u^o$ observations, the accuracy of analyzed u' is virtually unaffected, the accuracy of analyzed w' is decreased slightly, and the accuracy of analyzed v' is decreased substantially, but its sensitivity to Δx_c is not much affected expect for v' below z' = 1 km.

When the above $-u^o$ observations change to v^o observations, the CREs for u' are roughly tripled due to the absence of $-u^o$, as shown in rows 7–9 of Table 2, but the CREs for v' become nearly the same as those in rows 1–3 of Table 2 due to the presence of v^o. In this case, since the rapid variations of v' along x'-grid lines in the vortex core are analyzed by using Δx_c-dislocated VF-dependent background error covariance with v^o observations only, the analyzed v' in the vortex core becomes again more sensitive to Δx_c as shown by the rapid increase of CRE with Δx_c for v' in rows 7–9 of Table 2.

Figures 5a–d show that the analyzed $\mathbf{u}'$ and w' in E-v-T2 deviate from their respective benchmark fields again mainly in the vortex core but the u' deviations are increased outside the vortex core, especially at z' = 4 km in Fig. 5d, due to the absence of $-u^o$. The $\mathbf{u}'$ deviation is unchanged at the domain center but is changed to 9 (or 11) m s^{-1} southward at the benchmark vortex center in Fig. 5a (or Fig. 5c), which is slightly smaller than that in Fig. 2a (or Fig. 2c) because the analyzed vortex flow in the vortex core is slightly weakened due to the absence of $-u^o$. Again, linked via the mass

TABLE 3. As in Table 2, but from experiments performed with idealized Doppler scans of the eastward-slanted vortex in section 3b. In this case, E-uv-T0, E-u-T0, and E-v-T0 duplicate E-uv-1, E-u-1, and E-v-1 performed with the single-step approach in section 4b and listed in Table 4 of Part II.

		CRE (m s^{-1})			RCRE (%)		
Expt	Δx_c	u'	v'	w'	u'	v'	w'
E-uv-T0	0	0.8	0.6	1.4	5	4	15
E-uv-T1	$R_1/4$	1.3	1.8	1.9	8	12	20
E-uv-T2	$R_1/2$	2.1	3.1	2.7	14	20	28
E-u-T0	0	1.4	2.5	2.7	9	17	29
E-u-T1	$R_1/4$	2.3	3.9	4.3	15	25	46
E-u-T2	$R_1/2$	3.8	6.7	7.0	25	44	74
E-v-T0	0	As in Table 2					
E-v-T1	$R_1/4$	As in Table 2					
E-v-T2	$R_1/2$	As in Table 2					

continuity, the absence of $-u^o$ also causes the error of analyzed w' to increase slightly as shown in Figs. 5b and 5d versus Figs. 2b and 2d.

Figure 3c shows the AREs of analyzed (u', v', w') from E-v-T0, E-v-T1, and E-v-T2. Note again that the three green curves in Fig. 3c are very close to those in Fig. 3a, so the AREs for v' are nearly unaffected by the absence of $-u^o$. The thin red curves in Fig. 3c versus those in Fig. 3a show that the AREs for u' become substantially large due to the absence of $-u^o$, but the ARE increment caused by each increase of Δx_c is still small and is not much affected by the absence of $-u^o$. Thus, the analyzed u' is still not very sensitive (and much less sensitive than the analyzed v') to Δx_c due to the same reason as explained earlier in the first paragraph of section 3a(1). The three thick blue curves in Fig. 3c versus those in Fig. 3a show that the AREs for w' become large above $z' = 2$ km due to the absence of $-u^o$, but the ARE increment caused by each increase of Δx_c is still not large and is only slightly affected by the absence of $-u^o$. Thus, when the dual-Doppler ($-u^o$, v^o) observations reduce to single-Doppler v^o observations, the accuracy of analyzed v' is largely unaffected, and the accuracy of analyzed u' (or w') is decreased substantially (or moderately) but its sensitivity to Δx_c is not much affected by the absence of $-u^o$.

b. Results for slantwise vortex

For the three experiments performed with idealized ($-u^o$, v^o) observations of the eastward-slanted vortex, the CREs and RCREs of analyzed (u', v', w') are shown in rows 1–3 of Table 3. Here, the CRE (or RCRE) increases with Δx_c for each variable roughly in the same way as shown in rows 1–3 of Table 2 and described for the upright vortex in section 3a(1), so the sensitivities of dual-Doppler analyzed (u', v', w') to Δx_c are largely unaffected by the vortex slanting. The analyzed $\mathbf{u}'$ and w' at $z' = 1$ (or 4) km from E-uv-T2 (not shown) have nearly the same structures as those in Fig. 2a (or Fig. 2c) and their error fields have roughly the same main features as seen in Fig. 2b (or Fig. 2d) and explained in section 3a(1) for the upright vortex.

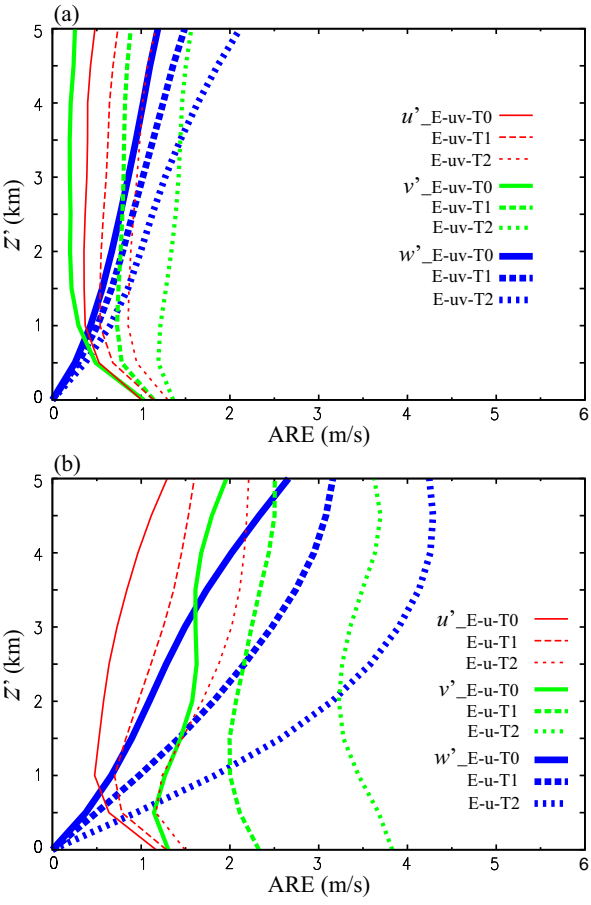

FIG. 6. As in Figs. 3a and 3b, but from the two sets of experiments performed in section 3b with idealized dual-Doppler ($-u^o$, v^o) observations and single-Doppler $-u^o$ observations of the eastward-slanted vortex.

The AREs of analyzed fields from this set of experiments are plotted in Fig. 6a. The three green curves in Fig. 6a are almost the same as those in Fig. 3a, so the AREs for v' are almost unaffected by the vortex eastward slanting. This is because the accuracy of analyzed v' depends mainly on v^o observations while the values of v^o on the coarse-resolution grid in (x', y', z') are unaffected by the vortex eastward slanting. The three red (or blue) curves in Fig. 6a versus those in Fig. 3a show that the AREs for u' (or w') are slightly increased (or decreased) due to the vortex eastward slanting, and this is because $-u^o$ contains a projection of the slantwise vertical velocity w' [see (2.2)–(2.3) of Part II] and therefore w' becomes partially observed but u' becomes less observed when the vortex is slanted eastward. Thus, when (u', v', w') are analyzed with the idealized ($-u^o$, v^o) observations, their accuracies and sensitivities to Δx_c are largely unaffected by the vortex slanting.

When the above $(-u^o, v^o)$ observations reduce to $-u^o$ observations, the CREs and RCREs of analyzed (u', v', w') in rows 4–6 of Table 2 change to those in rows 4–6 of Table 3. Here again, the CRE (or RCRE) increases with Δx_c for each variable roughly in the same way as shown in rows 4–6 of Table 2 and described for the upright vortex in section 3a(2), so the sensitivities of analyzed (u', v', w') to Δx_c are still largely unaffected by the vortex slanting. The analyzed $\mathbf{u}'$ and w' at $z' = 1$ (or 4) km from E-u-T2 (not shown) have roughly the same structures as those in Fig. 4a (or Fig. 4c) and their error fields have roughly the same main features as seen in Fig. 4b (or Fig. 4d) and explained in section 3a(2) for the upright vortex.

The AREs for (u', v', w') analyzed with $-u^o$ observations of the eastward-slanted vortex are shown in Fig. 6b. As shown, the three green curves in Fig. 6b have roughly the same magnitudes as those in Fig. 3b, so the AREs for v' are still not very much affected by the vortex eastward slanting in the absence of v^o. The three thin red curves in Fig. 6b versus those in Fig. 3b show that the ARE for u' is increased similarly in each experiment as the vortex becomes eastward slanted, and this can be explained by the less observed u' plus the absence of v^o. The three thick blue curves in Fig. 6b versus those in Fig. 3b show that when the vortex becomes eastward slanted, the ARE for w' is reduced slightly in E-u-T0 (because w' becomes partially observed as explained earlier) but increased (between $1 < z' < 4$ km) in E-u-T1 or E-u-T2 (due to the increased sensitivity of u' to Δx_c that increases the sensitivity of w' via the mass continuity). Thus, the analyzed (u', w') become slightly more sensitive to Δx_c due to the vortex eastward slanting.

As explained in section 3b(1), when the above $-u^o$ observations change to v^o observations of the eastward-slanted vortex, the values of v^o on the coarse-resolution grid in (x', y', z') are unaffected by the vortex eastward slanting, so the analyzed (u', v', w') are also unaffected by the vortex eastward slanting except that they are now located in the slantwise coordinates (x', y', z'). Thus, the CREs and RCREs in rows 7–9 of Table 3 for this set of experiments with the eastward-slanted vortex are the same as those in rows 7–9 of Table 2 for the set with the upright vortex.

4. Sensitivity experiments with pseudo-operational Doppler scans

a. *Results for upright vortex*

1) Experiments with pseudo-operational dual-Doppler observations

For the three experiments performed with pseudo-operational dual-Doppler scans of the upright vortex from radars A and B, the CREs and RCREs of analyzed (u', v', w') are shown in rows 1–3 of Table 4. As shown, when $\Delta\mathbf{x}_c$ increases from zero to $R_1\mathbf{e}/4$ (or $R_1\mathbf{e}/2$), the CRE is increased from 0.4 to 1.8 (or 3.4) m s^{-1} roughly by 340% (or 700%) for u', from 0.5 to 1.7 (or 3.3) m s^{-1} roughly by 280% (or 650%) for v', and from 1.9 to 3.7 (or 5.8) m s^{-1} roughly by 90% (or 200%) for w'.

TABLE 4. As in Table 2, but from experiments performed with pseudo-operational Doppler scans of the upright vortex in section 4a. Again, each experiment is named in three parts. The letter "AB," "A," or "B" in the middle part means that the experiment is performed with the dual-Doppler observations from radar A and radar B, the single-Doppler observations from radar A only, or the single-Doppler observations from radar B only. The letter "T0," "T1," or "T2" in the last part means that the experiment is performed by setting $\Delta\mathbf{x}_c = 0\mathbf{e}$, $R_1\mathbf{e}/4$, or $R_1\mathbf{e}/2$, where $\mathbf{e}$ is defined in (2.2) with $\Delta\mathbf{x}_c$ shown in Fig. 1. Thus, E-AB-T0, E-A-T0, and E-B-T0 are the control experiments that duplicate E-AB-1, E-A-1, and E-B-1 performed with the single-step approach in section 5a and listed in Table 6 of Part II.

		CRE (m s^{-1})			RCRE (%)		
Expt	$\Delta\mathbf{x}_c$	u'	v'	w'	u'	v'	w'
E-AB-T0	$0\mathbf{e}$	0.4	0.5	1.9	3	3	21
E-AB-T1	$R_1\mathbf{e}/4$	1.8	1.7	3.7	12	11	39
E-AB-T2	$R_1\mathbf{e}/2$	3.4	3.3	5.8	22	22	62
E-A-T0	$0\mathbf{e}$	0.6	2.2	2.9	4	14	31
E-A-T1	$R_1\mathbf{e}/4$	1.8	5.6	7.9	12	37	84
E-A-T2	$R_1\mathbf{e}/2$	3.5	10.3	14.2	22	67	151
E-B-T0	$0\mathbf{e}$	3.9	0.8	3.5	26	5	38
E-B-T1	$R_1\mathbf{e}/4$	5.7	2.1	5.8	37	14	62
E-B-T2	$R_1\mathbf{e}/2$	8.2	3.6	9.8	52	24	104

Here, the CREs increase with $\Delta\mathbf{x}_c$ faster than those from E-uv-T0 to E-uv-T2 in rows 1–3 of Table 2, and this can be explained by the following three reasons. (i) The starting CREs from E-AB-T0 in row 1 of Table 4 are substantially smaller than those from E-uv-T0 in row 1 of Table 2, because the pseudo-operational Doppler scans have denser data coverage than the idealized Doppler scans. (ii) As explained in section 3a(1), the deviation of $\mathbf{x}_c^e$ from $\mathbf{x}_c$ in the direction of $\Delta\mathbf{x}_c$ causes the error of analyzed $\mathbf{u}'$ to increase in the vortex core mainly in its $\Delta\mathbf{x}_c$-normal component. This error increases further when the rapid along-$\Delta\mathbf{x}_c$ variations of $\Delta\mathbf{x}_c$-normal component of $\mathbf{u}'$ in the vortex core are sampled more densely by the pseudo-operational Doppler scans but analyzed using the $\Delta\mathbf{x}_c$-dislocated VF-dependent background error covariance. (iii) The variations of $\Delta\mathbf{x}_c$ with z distort the vertical correlation structure of $\Delta\mathbf{x}_c$-dislocated VF-dependent background error covariance, and this causes additional analysis errors in the vortex core. Nevertheless, since the CREs for (u', v') started very small in E-AB-T0, their corresponding RCREs in Table 4 increase merely to 22% in E-AB-T2.

Figures 7a–d show that errors of analyzed $\mathbf{u}'$ and w' in E-AB-T2 are large in the vortex core but decrease rapidly away from the vortex core. In Fig. 7a (or Fig. 7c), the benchmark $\mathbf{u}'$ is about 30 (or 7) m s^{-1} southeastward at the domain center where the analyzed $\mathbf{u}'$ is constrained to vanish. The benchmark vortex center is denoted by the black dot at $(x', y') = -\Delta\mathbf{x}_c = (0.5, 0.3)$ km in Fig. 7a [or $(x', y') = -\Delta\mathbf{x}_c = (-0.08, 0.3)$ km in Fig. 7c], where the benchmark $\mathbf{u}'$ vanishes but

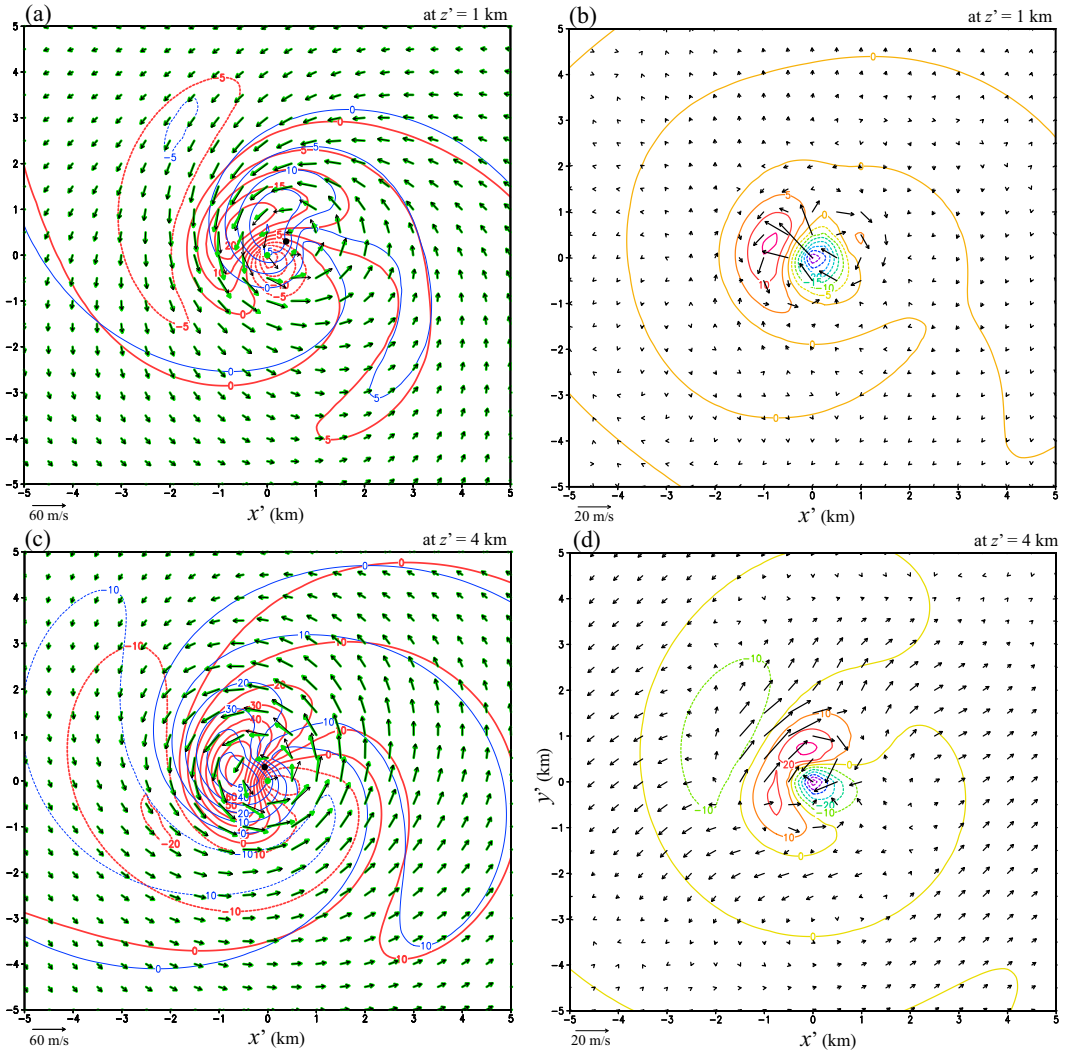

FIG. 7. As in Fig. 2, but from E-AB-T2 performed with pseudo-operational dual-Doppler observations of the upright vortex from radars A and B.

the analyzed $\mathbf{u}'$ is nonzero northwestward (or westward). Figure 7b shows that large $\mathbf{u}'$-vector errors in the vortex core are roughly perpendicular to $\Delta\mathbf{x}_c = (-0.5, -0.3)$ km at $z' = 1$ km, so they are mostly in the $\Delta\mathbf{x}_c$-normal direction due to the reason (ii) explained above. Figure 7d shows that large $\mathbf{u}'$-vector errors in the vortex core are mostly neither perpendicular nor parallel to $\Delta\mathbf{x}_c = (0.08, -0.3)$ km at $z' = 4$ km, so they are deviated away from the $\Delta\mathbf{x}_c$-normal direction due to the reason (iii) explained above. Also, at $z' = 4$ km, the $\mathbf{u}'$-vector errors in Fig. 7d decrease away from the vortex core not as rapidly as those in Fig. 2d, and this can be explained partially by the reason (iii) explained above and partially by the less observed (u', v') due to the increased slope angles of the radar beam and the reduced vertical resolutions of pseudo-operational Doppler observations at $z' = 4$ km.

The AREs from this first set of experiments are potted in Fig. 8a. As shown by the red (or green) curves in Fig. 8a, when $\Delta\mathbf{x}_c$ increases from zero to $R_1\mathbf{e}/4$ and then to $R_1\mathbf{e}/2$, the ARE for u' (or v') is increased roughly from 0.2 to 0.8 (or 0.6) m s^{-1} and then to 1.5 (or 1.2) m s^{-1} in the deep middle layer. The blue curves in Fig. 8a show that the ARE for w' is doubled (or tripled) roughly from 0.8 to 1.6 (or 2.4) m s^{-1} in the deep middle layer as $\Delta\mathbf{x}_c$ increases from zero to $R_1\mathbf{e}/4$ (or $R_1\mathbf{e}/2$). These results indicate that the analyzed (u', v') and w' remain adequately accurate outside the vortex core even when $\Delta\mathbf{x}_c$ increases to $R_1\mathbf{e}/2$.

2) EXPERIMENTS WITH PSEUDO-OPERATIONAL SINGLE-DOPPLER OBSERVATIONS

When the above dual-Doppler observations from radars A and B reduce to single-Doppler observations from radar A only, the CREs are nearly unchanged for u' but roughly doubled (or tripped) for w' (or v') in each experiment, as

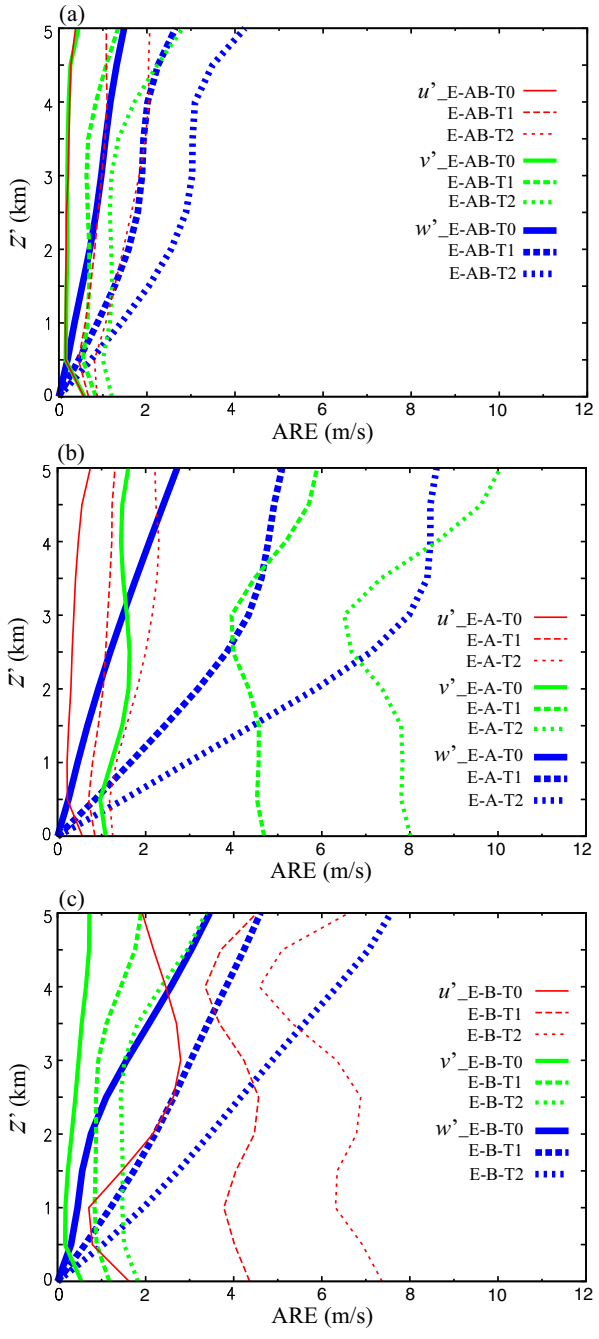

FIG. 8. As in Fig. 3, but from the three sets of experiments performed in section 4a with pseudo-operational Doppler observations of the upright vortex.

seen from rows 4–6 versus rows 1–3 in Table 4. The reduced accuracy of analyzed w' is caused indirectly via the mass continuity by the reduced accuracy of analyzed v' in each experiment, while the latter can be explained by the largely diminished projections of v' on v_r^o for single-Doppler observations from radar A. Here, the CREs are increased with $\Delta\mathbf{x}_c$ more rapidly than those in rows 4–6 of Table 2, and this can be explained again by the three reasons given in the previous subsection for the first set of experiments.

Figures 9a–d show that the analyzed $\mathbf{u}'$ (or w') from E-A-T2 deviates from its benchmark field significantly (or slightly) more than that from E-AB-T in Figs. 7a–d, and the $\mathbf{u}'$ deviations are mainly in v'-component velocities due to the absence of observations (mainly of v') from radar B (south of the vortex center). Figure 9b (or Fig. 9d) shows that large $\mathbf{u}'$-vector errors in the vortex core are still mostly in (or deviated away from) the $\Delta\mathbf{x}_c$-normal direction at $z' = 1$ (or 4) km similar to those in Fig. 7b (or Fig. 7d), but v'-component errors become large not only in the vortex core but also away from the vortex core due to the absence of observations from radar B.

The AREs from the above experiments are potted in Fig. 8b. The three thin red curves in Fig. 8b versus those in Fig. 8a show that the AREs for u' are nearly unaffected by the absence of observations from radar B. The three green curves in Fig. 8b versus those in Fig. 8a show that the AREs for v' are increased substantially due to the absence of observations from radar B. The three thick blue curves in Fig. 8b versus those in Fig. 8a show that the AREs for w' are also increased substantially due to the absence of observations from radar B. Thus, when the dual-Doppler observations from radars A and B reduce to single-Doppler observations from radar A only, the analyzed u' is nearly unaffected, but the analyzed v' and w' become substantially less accurate and more sensitive to $\Delta\mathbf{x}_c$.

When radar B is considered alone, the same behavior that is seen for radar A is replicated qualitatively except that the analyzed u' (instead of v') becomes much less accurate (see rows 7–9 versus rows 1–3 in Table 4) due to the absence of observations (mainly of u') from radar A (east of the vortex center). In this case, as shown in Figs. 10a–d, the analyzed $\mathbf{u}'$ (or w') from E-B-T2 deviates from its benchmark field significantly (or slightly) more than that from E-AB-T2 in Figs. 7a–d, and the $\mathbf{u}'$ deviations are mainly in u'-component velocities. Also, as shown in Fig. 10b (or Fig. 10d), large $\mathbf{u}'$-vector errors in the vortex core are mostly in (or partially deviated away from) the $\Delta\mathbf{x}_c$-normal direction at $z' = 1$ (or 4) km somewhat similar to those in Fig. 7b (or Fig. 7d), but u'-component errors become large nearly over the entire analysis domain due to the absence of observations from radar A.

The AREs from the experiments performed with single-Doppler observations from radar B are potted in Fig. 8c. As shown by the green curves and thin red (or thick blue) curves in Fig. 8c versus those in Fig. 8a, the AREs for v' are not much affected by the absence of observations from radar A, but the AREs for u' (or w') are increased substantially (or moderately) due to the absence of observations from radar A. Thus, when the dual-Doppler observations from radars A and B reduce to single-Doppler observations from radar B only, the analyzed v' is not much affected, but analyzed u' (or w') becomes substantially (or moderately) less accurate and more sensitive to $\Delta\mathbf{x}_c$.

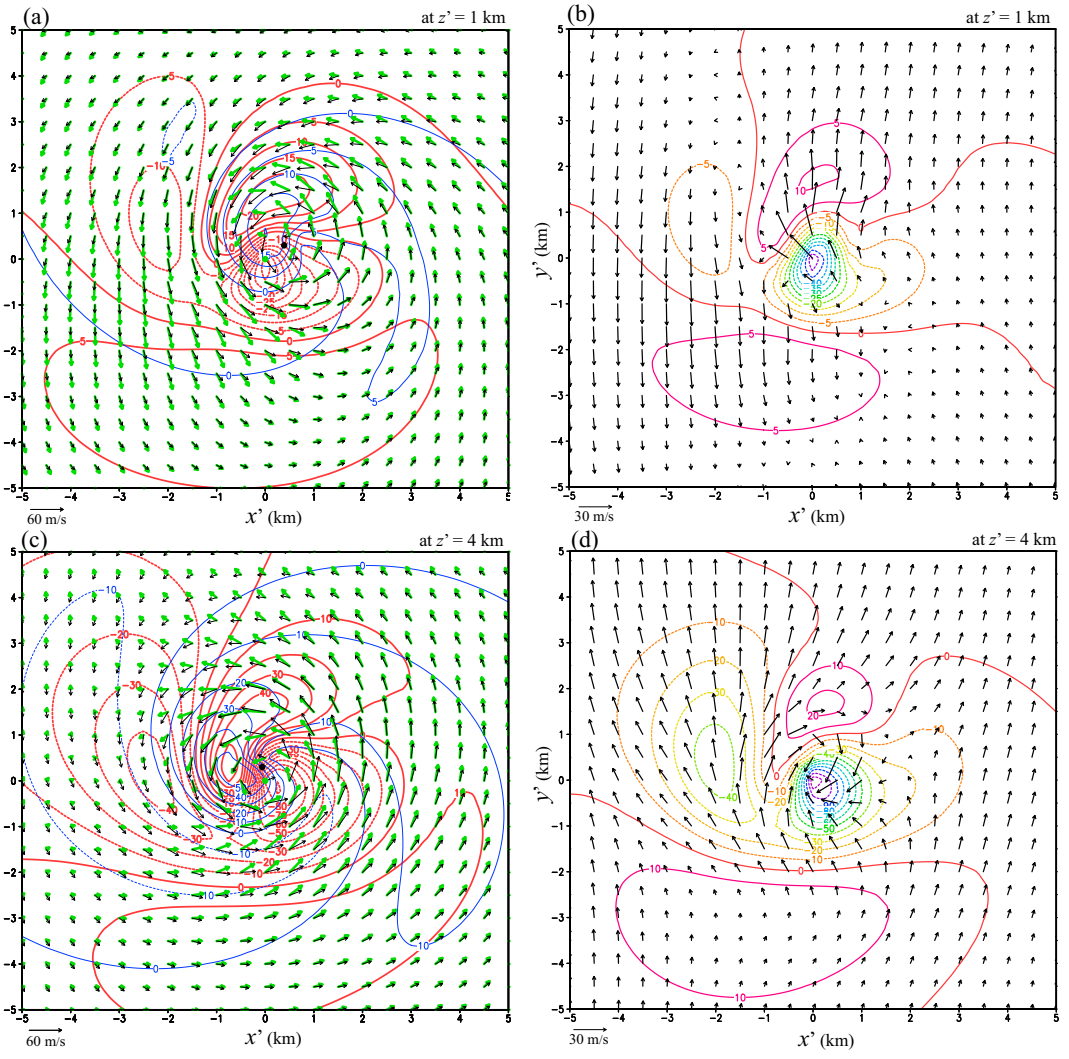

FIG. 9. As in Fig. 7, but from E-A-T2 performed with pseudo-operational single-Doppler observations of the upright vortex from radar A only.

b. Results for slantwise vortex

For the three experiments performed with pseudo-operational dual-Doppler observations of the eastward-slanted vortex, the CREs and RCREs of analyzed (u', v', w') are listed in rows 1–3 of Table 5. By comparing the listed values with those in rows 1–3 of Table 4, it is easy to see that the accuracies of analyzed (u', v', w') and their sensitivities to $\Delta\mathbf{x}_c$ are nearly unaffected by the vortex slanting. This is seen more clearly from the AREs plotted in Fig. 11a for this set of experiments versus those in Fig. 8a with the upright vortex. Thus, the accuracies and sensitivities of analyzed (u', v', w') to $\Delta\mathbf{x}_c$ are nearly unaffected by the vortex slanting.

When the above dual-Doppler observations reduce to single-Doppler observations from radar A only, the values of CREs and RCREs in rows 1–3 of Table 5 are changed to those listed in rows 4–6 of Table 5. As these changes are quite similar to those in Table 4 for the upright vortex, the sensitivities of analyzed (u', v', w') to $\Delta\mathbf{x}_c$ are not much affected by the vortex slanting. This is also seen from the AREs plotted in Fig. 11b versus those in Fig. 8b. Thus, when the dual-Doppler observations reduce to single-Doppler observations from radar A only, the sensitivities of analyzed (u', v', w') to $\Delta\mathbf{x}_c$ are still not much affected the vortex slanting.

The above insensitivities to the vortex slanting are seen similarly when radar B is considered alone. This is indicated by the listed values of CREs and RCREs in rows 7–9 of Table 5 versus those in rows 7–9 of Table 4, and is also seen more clearly from the AREs plotted in Fig. 11c versus those in Fig. 8c.

5. Conclusions

In this paper, four groups of numerical experiments are designed and performed to examine the sensitivities of

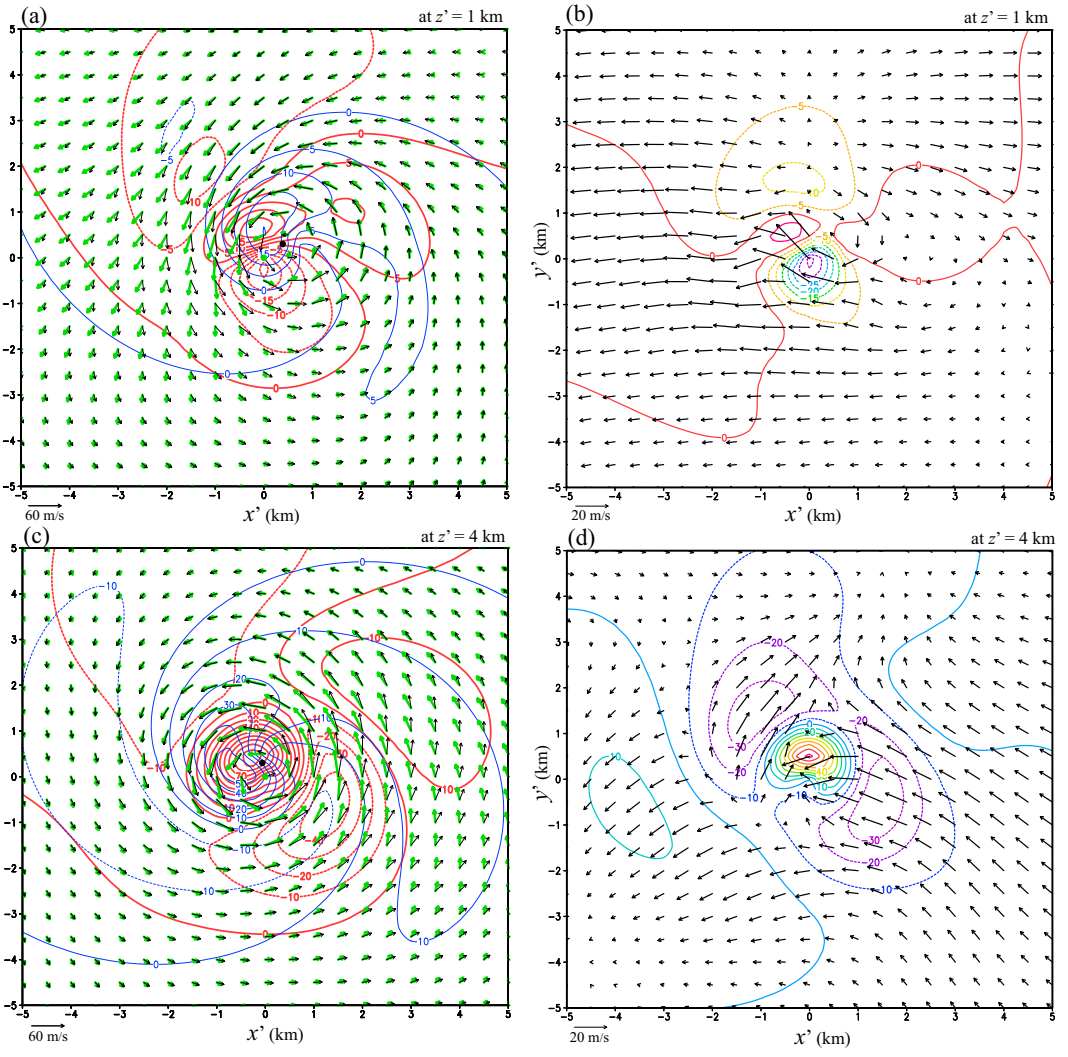

FIG. 10. As in Fig. 7, but from E-B-T2 performed with pseudo-operational single-Doppler observations of the upright vortex from radar B only.

analyzed velocity (u', v', w') of vortex flow (VF) in the vortex-following coordinate system (x', y', z') produced by the VF-Var (formulated in Part I) to small errors in the estimated vortex center locations. Each group consists of three sets (with one set for dual-Doppler analysis and the remaining two sets for single Doppler analyses), and each set consists of one control experiment and two test experiments. In each control experiment, the estimated vortex center axis is assumed to be error-free as in Part II. In the first (or second) group, simulated radial-velocity observations are generated by idealized Doppler scans of upright (or eastward slantwise) vortex as in Part II, but the estimated vortex center axis has a vertically uniform and x-directional error of $\Delta x_c = R_1/4$ (or $R_1/2$) in the first (or second) test experiment, where R_1 is the radius of vortex core. In the third (or fourth) group, simulated radial-velocity observations are generated by pseudo-operational Doppler scans of upright (or eastward slantwise) vortex as in Part II, but the estimated vortex center axis has a vertically variable vector error of $\Delta\mathbf{x}_c = R_1\mathbf{e}/4$ (or $R_1\mathbf{e}/2$) in the first (or second) test experiment, where $\mathbf{e}$ is a smooth vector function of height defined in (2.2) and shown in Fig. 1.

The results from these experiments are summarized below:

1) The increase of $|\Delta\mathbf{x}_c|$ (from 0 to $R_1/2$) causes large analysis error increases in the vortex core but the increased analysis errors decrease rapidly away from the vortex core especially for dual-Doppler analyses.
2) The increased errors of analyzed $\mathbf{u}' \equiv (u', v')$ in the vortex core are mainly in the $\Delta\mathbf{x}_c$-normal component, because this component varies much more rapidly than the other component along the $\Delta\mathbf{x}_c$ direction in the vortex core.
3) As the rapid along-$\Delta\mathbf{x}_c$ variations of $\Delta\mathbf{x}_c$-normal component of $\mathbf{u}'$ in the vortex core are sampled more densely

TABLE 5. As in Table 4, but from experiments performed with pseudo-operational Doppler scans of eastward-slanted vortex in section 4b. In this case, E-AB-T0, E-A-T0, and E-B-T0 duplicate E-AB-1, E-A-1, and E-B-1 performed with the single-step approach in section 5b and listed in Table 8 of Part II.

		CRE (m s^{-1})			RCRE (%)		
Expt	$\Delta\mathbf{x}_c$	u'	v'	w'	u'	v'	w'
E-AB-T0	0**e**	0.5	0.4	1.5	4	3	16
E-AB-T1	R_1**e**/4	1.8	1.6	3.3	12	10	35
E-AB-T2	R_1**e**/2	3.5	3.1	5.8	22	20	61
E-A-T0	0**e**	0.9	2.4	2.6	6	16	28
E-A-T1	R_1**e**/4	3.0	6.1	7.2	19	40	77
E-A-T2	R_1**e**/2	5.1	11.2	12.0	32	73	127
E-B-T0	0**e**	3.9	0.8	3.4	26	6	36
E-B-T1	R_1**e**/4	5.5	2.4	5.5	35	16	59
E-B-T2	R_1**e**/2	7.9	4.1	9.3	50	27	99

(in lower elevations by the pseudo-operational Doppler scans) but analyzed using the $\Delta\mathbf{x}_c$-dislocated VF-dependent background error covariance, the analysis errors for the $\Delta\mathbf{x}_c$-normal component of $\mathbf{u}'$ can become slightly larger in the vortex core.

4) The vertical variations of $\Delta\mathbf{x}_c$ distort the vertical correlation structure of $\Delta\mathbf{x}_c$-dislocated VF-dependent background error covariance. This also increases the analysis errors in the vortex core.
5) The dual-Doppler analyses have adequate accuracies outside the vortex core even when $\Delta\mathbf{x}_c$ increases to $R_1\mathbf{e}/2$ (see Figs. 7 and 8a), while single-Doppler analyses can also have adequate accuracies outside the vortex core mainly for the single-Doppler-observed velocity component (see Figs. 9, 10, and 8b–c).
6) The above results are largely unaffected by the vortex slanting (see Fig. 11 versus Fig. 8).

The above summarized results address the issue raised in the introduction concerning the sensitivities of the analyses produced by the VF-Var to small errors in estimated vortex center locations. This issue is important for applying the VF-Var to real Doppler-velocity observations of tornadic mesocyclones, because the vortex center location (estimated by using the three-step method of Xu et al. 2017) is not error-free (due to the limited spatial and temporal resolutions of radar scans and the intrinsic uncertainty of true vortex center) although the error can be only a fraction of the radius of vortex core. The results obtained in this paper are important and will be used for assessing the accuracies of different velocity components inside and outside the vortex cores in analyzed VF fields obtained by applying the VF-Var to real radar observations to gain physical insights on VF structures in tornadic mesocyclones. The assessed accuracies should have important applications for properly specifying the error variances of VF-Var analyzed vortex winds when these analyzed winds are used as "observations" in data assimilation to improve the small-scale vortex wind analyses (as mentioned in the introduction section). Results from continued research in this direction will be reported in follow-up papers.

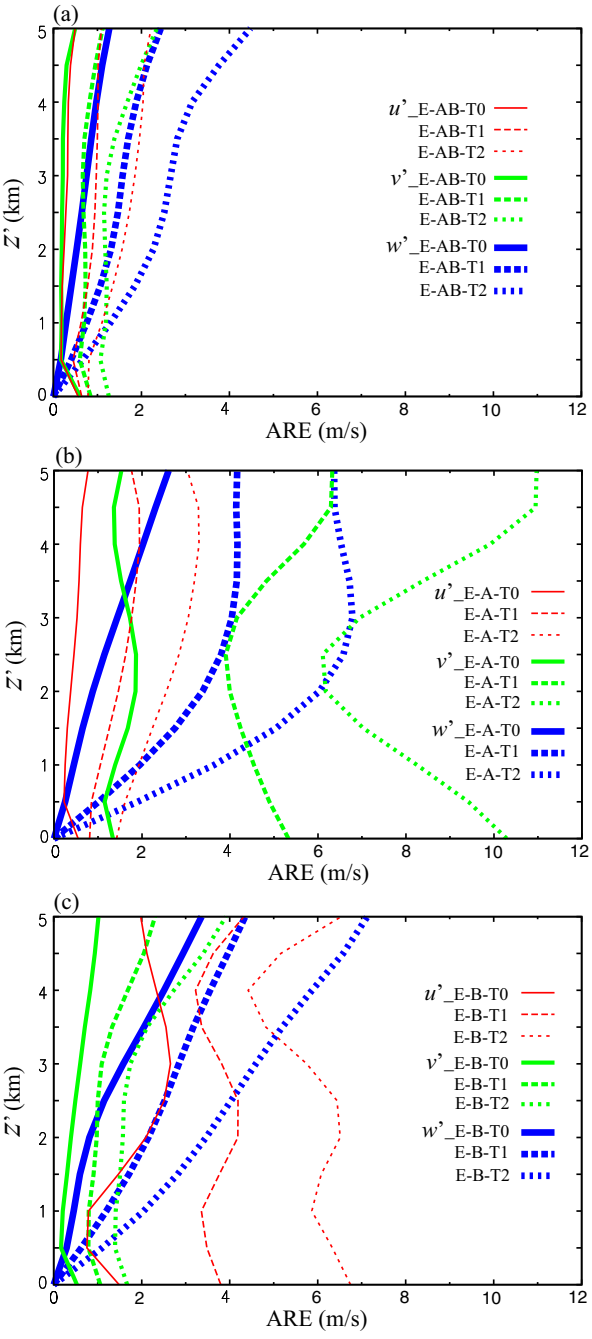

FIG. 11. As in Fig. 3, but from the three sets of experiments performed in section 4b with pseudo-operational Doppler observations of the eastward-slanted vortex.

Acknowledgments. We thank Jidong Gao and three anonymous reviewers for providing many constructive comments and detailed suggestions. The numerical experiments were performed at the OU Supercomputing Center for Education and Research. The research work was supported by the NSSL Warn-on-Forecast project and the Office of Naval Research under Award N000142012449 to the University of

Oklahoma (OU). Funding was also provided by NOAA/Office of Oceanic and Atmospheric Research under NOAA–OU Cooperative Agreement NA16OAR4320072, U.S. Department of Commerce.

Data availability statement. No real radar wind data are used in this study. All the wind data experimented in this study were generated from the theoretical formulations published in Part I and Part II.

REFERENCES

Gao, J., and D. Stensrud, 2014: Some observing system simulation experiments with a hybrid 3DEnVAR system for storm-scale radar DA. *Mon. Wea. Rev.*, **142**, 3326–3346, https://doi.org/10.1175/MWR-D-14-00025.1.

——, and Coauthors, 2013: A real-time weather-adaptive 3DVAR analysis system for severe weather detections and warnings. *Wea. Forecasting*, **28**, 727–745, https://doi.org/10.1175/WAF-D-12-00093.1.

Jones, T. A., K. Knopfmeier, D. Wheatley, G. Creager, P. Minnis, and R. Palikonda, 2016: Storm-scale DA and ensemble forecasting with the NSSL experimental Warn-on-Forecast system. Part II: Combined radar and satellite data experiments. *Wea. Forecasting*, **31**, 297–327, https://doi.org/10.1175/WAF-D-15-0107.1.

Lawson, J. R., J. S. Kain, N. Yussouf, D. C. Dowell, D. M. Wheatley, K. H. Knopfmeier, and T. A. Jones, 2018: Advancing from convection-allowing NWP to Warn-on-Forecast: Evidence of progress. *Wea. Forecasting*, **33**, 599–607, https://doi.org/10.1175/WAF-D-17-0145.1.

Skinner, P. S., and Coauthors, 2018: Object-based verification of a prototype Warn-on-Forecast system. *Wea. Forecasting*, **33**, 1225–1250, https://doi.org/10.1175/WAF-D-18-0020.1.

Snook, N., M. Xue, and Y. Jung, 2019: Tornado-resolving ensemble and probabilistic predictions of the 20 May 2013 Newcastle–Moore EF5 tornado. *Mon. Wea. Rev.*, **147**, 1215–1235, https://doi.org/10.1175/MWR-D-18-0236.1.

Stensrud, D. J., and Coauthors, 2009: Convective-scale Warn-on-Forecast system: A vision for 2020. *Bull. Amer. Meteor. Soc.*, **90**, 1487–1500, https://doi.org/10.1175/2009BAMS2795.1.

——, and Coauthors, 2013: Progress and challenges with Warn-on-Forecast. *Atmos. Res.*, **123**, 2–16, https://doi.org/10.1016/j.atmosres.2012.04.004.

Wang, Y., J. Gao, P. S. Skinner, K. Knopfmeier, T. Jones, G. Creager, P. L. Heiselman, and L. J. Wicker, 2019: Test of a weather-adaptive dual-resolution hybrid Warn-on-Forecast analysis and forecast system for several severe weather events. *Wea. Forecasting*, **34**, 1807–1827, https://doi.org/10.1175/WAF-D-19-0071.1.

Wheatley, D. M., K. H. Knopfmeier, T. A. Jones, and G. J. Creager, 2015: Storm-scale DA and ensemble forecasting with the NSSL experimental Warn-on-Forecast system. Part I: Radar data experiments. *Wea. Forecasting*, **30**, 1795–1817, https://doi.org/10.1175/WAF-D-15-0043.1.

Xu, Q., 2021: A variational method for analyzing vortex flows in radar scanned tornadic mesocyclones. Part I: Formulations and theoretical considerations. *J. Atmos. Sci.*, **78**, 825–841, https://doi.org/10.1175/JAS-D-20-0158.1.

——, and L. Wei, 2021: A variational method for analyzing vortex flows in radar-scanned tornadic mesocyclones. Part II: Tests with analytically formulated vortices. *J. Atmos. Sci.*, **78**, 843–861, https://doi.org/10.1175/JAS-D-20-0159.1.

——, ——, W. Gu, J. Gong, and Q. Zhao, 2010: A 3.5-dimensional variational method for Doppler radar data assimilation and its application to phased-array radar observations. *Adv. Meteor.*, **2010**, 797265, https://doi.org/10.1155/2010/797265.

——, ——, and K. Nai, 2015a: Analyzing vortex winds in radar observed tornadic mesocyclones for nowcast applications. *Wea. Forecasting*, **30**, 1140–1157, https://doi.org/10.1175/WAF-D-15-0046.1.

——, ——, ——, S. Liu, R. M. Rabin, and Q. Zhao, 2015b: A radar wind analysis system for nowcast applications. *Adv. Meteor.*, **2015**, 264515, https://doi.org/10.1155/2015/264515.

——, ——, and ——, 2017: A three-step method for estimating vortex center locations in four-dimensional space from radar observed tornadic mesocyclones. *J. Atmos. Oceanic Technol.*, **34**, 2275–2281, https://doi.org/10.1175/JTECH-D-17-0123.1.

Yussouf, N., J. S. Kain, and A. J. Clark, 2016: Short-term probabilistic forecasts of the 31 May 2013 Oklahoma tornado and flash flood event using a continuous-update-cycle storm-scale ensemble system. *Wea. Forecasting*, **31**, 957–983, https://doi.org/10.1175/WAF-D-15-0160.1.

——, T. A. Jones, and P. K. Skinner, 2020: Probabilistic high-impact rainfall forecasts from landfalling tropical cyclones using Warn-on-Forecast system. *Quart. J. Roy. Meteor. Soc.*, **146**, 2050–2065, https://doi.org/10.1002/qj.3779.